Shear Thinning and Tumbling Dynamics of Single Polymers in the Flow-Gradient Plane

Rodrigo E. Teixeira,[†,‡,§] Hazen P. Babcock,[‡,⊥] Eric S. G. Shaqfeh,[†,∥,#] and Steven Chu[*,‡]

Department of Chemical Engineering, Stanford University, Departments of Physics and Applied Physics, Stanford University, and Department of Mechanical Engineering, Stanford University, Stanford, California 94305

Received September 16, 2004; Revised Manuscript Received November 2, 2004

ABSTRACT: The conformational changes imparted on single, flexible DNA polymers by a steady, simple shear flow were directly visualized in the flow-gradient plane. Two fluorescently stained DNA double-strand sizes of 22 μm and 80 μm in contour length were employed, and Wi values of up to 584 were probed (Wi = shear rate × longest polymer relaxation time). By exploitation of the linear proportionality between polymer density and its recorded image, the accessible radius of gyration tensor elements (G_{ij}) were measured. Of those, the ensemble-averaged $\langle G_{22}\rangle$ and $\langle G_{12}\rangle$ were related to the bulk shear viscosity and first normal stress coefficient, respectively, via the Giesekus stress tensor. We found their respective behaviors to follow power-law decays of $Wi^{-0.52}$ and $Wi^{-1.28}$ at large Wi. Polymer dynamics were also investigated. Like rigid ellipsoids of revolution, polymers displayed a constant partition between positive and negative orientations irrespective of shear rate at $Wi \gg 1$. Unlike them, however, polymers preferred positive orientations, spending there ∼ 75% or their time vs 50% for rigid ellipsoids. End-over-end tumbling was observed, confirming a long-standing prediction and numerous single-chain computer simulation studies. The tumbling frequency followed $Wi^{0.62}$, and an equation was derived from simple advection and diffusion arguments to reproduce these observations.

Introduction

Near a solid boundary, any arbitrary flow field is nearly a shear flow and, as such, shear flow is nearly omnipresent. For any flow, a simple Newtonian fluid can be transformed into an interesting nonlinear material with a deformation history-dependent behavior by adding trace amounts of polymer. For polymers in shear flow, shear rate-dependent viscosity, normal stresses, and elastic instabilities[1,2] are found. This complex behavior arises from microscopic stresses caused by each polymer chain as the flow perturbs the chain conformation away from the equilibrium state. Bulk rheometry experiments dating back several decades identified two major properties of dilute polymer solutions, a shear viscosity and a first normal stress difference. Both properties demonstrate shear thinning beyond a certain characteristic shear rate as the shear rate is increased.[3] Even though the flow-gradient projected polymer dimensions are the molecular underpinnings for understanding complex fluid behavior, they have heretofore only been measured indirectly and only as ensemble-averaged quantities.[4−10]

The dynamics of flexible and dilute polymers in simple shear flow have also been the subject of much interest.[11−22] Several long-standing predictions were verified experimentally including a key concept put forth by Lumley[22] and deGennes,[16] who both argued that the rotational component or vorticity of a simple shear flow forces polymers to "tip over" or "tumble", thus preventing them from ever reaching a steady-state conformation. Only relatively recently were single polymers in shear flow visualized for the first time.[23,24] Both of these studies illuminated the flow-vorticity plane and revealed the presence of continuous and dramatic conformation fluctuations. Computer simulation studies have suggested that flow and vorticity excursions must be linked via fluctuations in the shear-gradient direction.[25−28] Since the gradient dimension was hidden from view in the orthogonal direction of these single polymer visualizations, only indirect comparisons with simulated model polymers were possible.[28,29] Thus, the observation of single polymer conformation changes, in the gradient and flow directions under an applied simple shear flow remains of great interest.

Experimental Section

Apparatus. Simple shear flow was generated between two parallel microscope slides resting upright along the slide's long (3 in. by 1 mm) edge on top of a coverslip (Figure 1, parts A and B). A constant gap, h, between the slides, or shearing surfaces, was determined by a thin sheet of mica glued to one of the surfaces at ∼ 2 mm above the coverslip. Two feedback-controlled motors (Oriel) were used to drive the apparatus. One motor translated one of the shearing surfaces at a constant speed, v, relative to the other, setting the shear rate, $\dot{\gamma} = v/h$. The slowly moving surface was spring-loaded in the vertical and horizontal directions to stabilize the gap during translation. By translating the entire flow assembly in the opposite direction using the second motor, we were able to track the fluorescing double-stranded DNA molecule of interest (described below) without perturbing the shear rate for a time t corresponding to a few hundred units of shear strain ($\dot{\gamma}t$).

We measured the properties of the generated flow by tracking the movements of 1 μm green fluorescent beads (Duke

* To whom correspondence should be addressed. E-mail: schu@stanford.edu.
[†] Department of Chemical Engineering, Stanford University.
[‡] Departments of Physics and Applied Physics, Stanford University.
[§] E-mail: teixeira@stanford.edu.
[⊥] Present address: Department of Chemistry and Chemical Biology, Harvard University, Cambridge, MA 02138 E-mail: hbabcock@fas.harvard.edu.
[∥] Department of Mechanical Engineering, Stanford University.
[#] E-mail: eric@chemeng.stanford.edu.

10.1021/ma048077l CCC: $30.25
Published on Web 12/30/2004

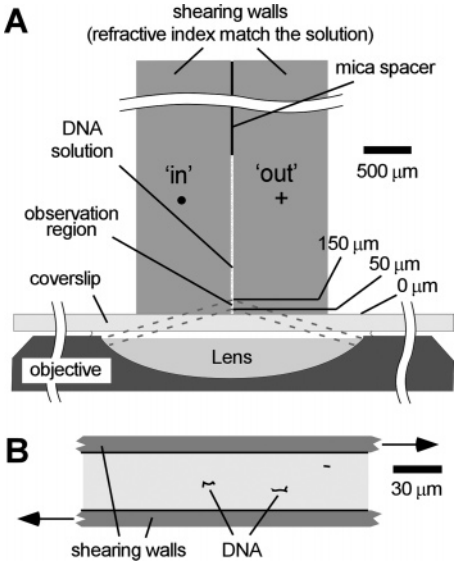

Figure 1. (A) Drawn to scale schematic representation of the experimental arrangement. Shear flow was generated between two quartz microscope slides, shown as gray rectangles driven "in" and "out" of the plane of the paper by the rest of the apparatus (not shown), and separated by 34 μm with a mica sheet spacer. The bottom, as well as the inner surfaces of the slides were polished to optical quality to ensure a smooth flow and prevent the formation of air pockets which could distort the image. DNA was epi-illuminated and imaged from below with a 1.45 NA 63× oil immersion objective (Olympus) at distances farther than 50 μm away from the coverslip, where the shear rate became constant. Image distortions caused by the refraction of fluorescence light at the solution−quartz interface were eliminated by tuning the sucrose and glucose concentrations such that the refractive index of solution matched that of quartz. Images were detected by a Micromax 512BFT CCD video camera (Roper Scientific). The sampling rate was 2 Hz. (B) Schematic where, during data acquisition, DNA is kept stationary with respect to the CCD detector while the shearing walls move in opposite directions at a constant relative speed.

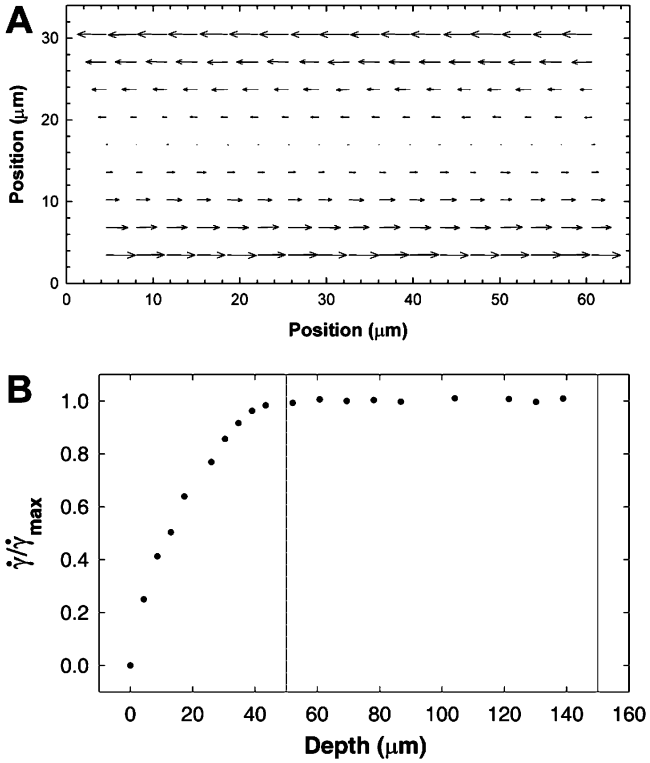

Figure 2. (A) Velocity field reconstructed from the movements of 1 μm green fluorescent beads at various depths. Shown here is a depth of 50 μm and $\dot{\gamma} = 1.0\ s^{-1}$. Each arrow is an average over 30 to 50 velocity vectors. (B) Shear rate as a function of depth or distance from the bottom coverslip. The shear rate was found from bead tracking data by fitting a line to the flow component of the bead velocity vs the position along the gradient of shear direction. When close to the coverslip the velocity gradient varies along the gradient direction due to the no slip boundary condition but becomes constant as the shear rate plateaus above ~45 μm. Values are averages over ~100 strains at each focal depth. The vertical gray lines mark the minimum experimental depth and the maximum working distance permitted by the objective.

Scientific). The shear rate rose from zero at the bottom (coverslip) surface to a constant value at a height above ~45 μm (Figure 2A), where the flow matched a simple linear shear (Figure 2B). Data were collected from molecules residing between ~50 and 150 μm from the coverslip surface. As indicated in Figure 1, most of the light collected by the microscope objective passed through the fused quartz shearing walls. To eliminate optical distortions at the fluid-quartz interface, the index of refraction of both media were matched (to $n = 1.458$) by adjusting the total glucose plus sucrose concentration in aqueous solution to 67.1% (w/w). We extracted shear rates for several wall translation speeds and found the relationship to be linear, as expected, and calculated the gap = slope^{-1} = 34 μm. This value was independently verified several times by direct visualizations of the gap at different positions along the length of the slide. We translated the shearing surface at speeds varying from 2 to 80 μm/s, thus producing shear rates from 0.058 to 2.33 s^{-1} with <5% root-mean-squared (RMS) fluctuations.

Optics. Imaging and detection was done by standard epi-microscopy optics coupled to a CCD camera. Molecules were epi-illuminated by a 100 W mercury arc lamp (100HBOW/2, Zeiss, Thornwood, NY), after a 480 ± 20 nm band-pass excitation filter and a 505 nm long pass dichroic mirror. Light was collected by a 1.45 NA, 63x oil immersion Planapo objective (Olympus, Melville, NY) with a 535 ±25 nm emission filter (Filter set 41001, Chroma, Brattleboro, VT) and a 300 mm achromatic doublet tube lens (Newport, Irvine, CA). Detection was done by a nonintensified Micromax 512BFT (back-illuminated frame transfer) CCD camera (Roper Scientific), which is able to maintain a <1.5% deviation from a linear response across a dynamic range 2 orders of magnitude greater than needed. The linearity of the camera proved critical to obtaining accurate measurements of molecular dimensions. A preliminary test with a microchannel plate light amplifier coupled to the CCD yielded distorted images, compared to the linear CCD, as the light impacting a given pixel leaked onto neighboring pixels (a process known as "fluorescent blooming"). This artifact, while negligible for polymer extension measurements, becomes significant when determining submicrometer dimensions such as the polymer's thickness in shear flow. The resolving power of our microscope was 0.25−0.3 μm. To obtain adequate imaging, the total magnification was adjusted such that the length per pixel was ~$^1/_2$ of the resolution. The sampling rate throughout the experiments was 2 Hz.

Materials. We employed two double-stranded DNA sizes. When stained with YOYO-1 (Molecular Probes), their contour lengths were measured at 22 μm (λ-DNA, Gibco BRL) and 80 μm (graciously donated by US Genomics). The 80 μm DNA sample is roughly 185-Kbp (±5%) in length and was purified by pulsed-field gel electrophoresis after a restriction digest of bacterial artificial chromosome amplified plasmids. The fluorescent dye intercalates between stacked base-pairs at about one dye per four bases. This increases the persistence length of DNA from ~53 nm in the native state[30] to ~66 nm.[31] The resulting fluorescent polymers thus contained ~330 and ~1210 persistence lengths.

The DNA was contained in a buffer solvent designed to preserve fluorophore brightness for at least twice as long as the duration of our experiments and to protect strands from cleavage by oxidizing agents. Still, as an extra precaution all

molecules were inspected for possible fragmentation by comparing their individual total brightness to known standards. The solvent contained 10 mM Tris buffer pH 8.0, 10 mM NaCl, 1 mM EDTA and 67.1% (w/w) sucrose. To retard photobleaching, an oxygen scavenging mixture of glucose (10% w/v), glucose oxidase (0.05 mg/mL), catalase (0.01 mg/mL), and β-mercaptoethanol (1% v/v) was added to the solvent. A solvent viscosity of 300 cP was measured with an Ares rheometer (Rheometric Scientific) equipped with a water bath running at the experimental temperature of 17 °C. Before each experiment, the sugar concentration in the buffer was verified to within 0.1% ($\Delta n < 0.0002$) of the target concentration for index matching. About 7 mL of sample was deposited onto the flow cell and allowed to settle. To prevent evaporation, a layer of mineral oil was dispensed over the sample. In this manner the viscosity, as well as the refractive index, was maintained constant throughout the experiment.

Experimental Procedures. The shear rate was made dimensionless by expressing $\dot{\gamma}$ as the Weissenberg number $Wi = \dot{\gamma}\tau$, where τ is the longest polymer relaxation time. We measured τ by timing the relaxations of several partially stretched, identical molecules and averaging. For each molecule, the polymer extension or stretch, $x(t)$, was recorded after the flow was stopped. Then, the function $x(t)^2 = a + b \exp(-t/\tau)$ was fit for each configuration trajectory over $x/L < 0.3$, where L is the contour length, and a, b and τ are free parameters. The average values thus obtained were $\tau = 28$ s for the 22 μm DNA (λ-phage DNA) and $\tau = 251$ s for the 80 μm piece, both in the 300-cP solvent. These values are in the ratio of $L^{1.68}$, which is consistent with the 1.66 ± 0.10 exponent found in a DNA relaxation study[32] and previous λ-phage DNA experiments at different solvent viscosities.[23,33−35] Thus, by adjusting the applied shear rate our experiments were conducted in the range $0 \leq Wi \leq 49$ with the 22 μm DNA and $0 \leq Wi \leq 584$ with the 80 μm DNA.

The transient conformational changes as the molecule unraveled from a coiled state immediately after the onset of flow typically lasted <70 strains. These data were not used in this study (The behavior of the startup of shear was the subject of two previous papers[28,29]). Molecules chosen at random were followed for ~ 40 to 360 strain units beyond the initial 70 strain and for a time long enough to capture several end-to-end conformation fluctuations per molecule.

We eliminated polymer−polymer interactions by working with dilute solutions of $10^{-5}c^*$ (where c^* is the overlap concentration) while also visually selecting out any close encounters between two or more polymers. Finally, we minimized polymer−wall hydrodynamic interactions by selecting chains near the gap center. Woo et al.[36] recently characterized wall-effects on the chain gradient thickness under shear flow. Those effects were found significant only for thin gaps ($h \leq R_G$) and negligible for $h \gg R_G$. For our largest polymer, $h/R_G = 25$. The contour length, albeit larger than the gap, was not the relevant length scale for gauging the influence of the shearing walls.

Single Molecule Measurements. Each recorded movie of DNA motion was first analyzed using custom-made automatic image recognition software and then reviewed manually for possible errors. For every frame two separate data sets were extracted. The first quantity extracted was the maximum chain *extension* projected onto the shear flow direction (x). As a clarification we point out that x is not the end-to-end distance commonly used in chain statistics since the polymer ends could not be resolved with our optical setup whenever the molecule was coiled.

The second set of quantities extracted were the components of the radius of gyration tensor, defined as

$$G_{ij} \equiv \frac{\sum_{p,q} I(p,q) \cdot R_i^{p,q} R_j^{p,q}}{\sum_{p,q} I(p,q)}$$

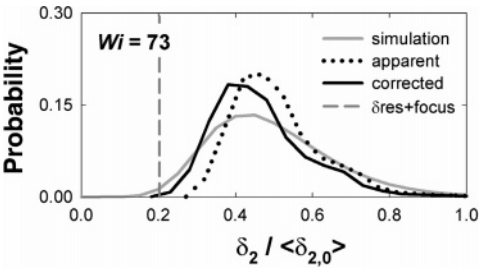

Figure 3. Histograms of polymer thickness (δ) before (dotted) and after (black) deconvoluting, or correcting the raw apparent polymer thickness data with $\delta_2 = \sqrt{\delta_{2,\text{apparent}}^2 - \delta_{\text{res+focus}}^2}$, where $\delta_{\text{res+focus}} = 0.16$ μm (vertical dashed line). Also shown, for comparison, is BD simulation data with hydrodynamic interactions and excluded volume forces from ref 38 (gray). The bin size is 0.05 μm.

where I is the 2-dimensional polymer image, $I(p,q)$ gives the intensity of the pixel in the pth column and qth row above the background level, and $R_i^{p,q}$ denotes the distance in the ith direction from the center-of-mass of the polymer to the pth column and qth row pixel. Defining the shear flow direction to be the "1"-direction, and the transverse direction along the gradient of shear to be the "2"-direction, the radius of gyration tensor elements made visible in the flow-gradient plane are G_{11}, G_{22}, and $G_{12} = G_{21}$.

Our measure of G_{ij} only differs from the theoretical definition in that the summation over the polymer contour is replaced with the summation over the polymer's image. The replacement, however, is inconsequential since any given pixel detects a signal that corresponds linearly to the mass of polymer found at that position. This occurs because (i) staining is uniform along the DNA contour at the optical resolution, (ii) the entire molecule fits inside the depth of focus, and (iii) the camera's response is linear (between the intensity of light illuminating each pixel and their respective final digital readouts, as described previously).

From our knowledge of G_{11}, G_{22}, and $G_{12} = G_{21}$, two additional parameters were calculated: the configuration *thickness* (δ_2) in the gradient of shear direction and the configuration *orientation* relative to the flow direction (θ). These are defined as follows:

$$\delta_2 = \sqrt{G_{22}}$$

$$\tan 2\theta = \frac{2G_{12}}{G_{11} - G_{22}}$$

Angles were chosen to be positive when measured from the flow ("1") axis toward the positive gradient ("2") axis in the flow-gradient plane (see Figure 4).

The accuracy of our polymer measurements becomes increasingly poor as the length of interest approaches the resolution limit of the collected light (509 nm). Such is the case in our thickness measurements, δ_2. This limitation is inherent in the optical microscopy technique and does not depend on image magnification. Because the created image is the result of the real object convoluted with the microscope's point-spread function,[37] objects appear larger than their true sizes. Fortunately, we can correct for this positive bias by measuring the same effect on objects of known size and shape. We measured the apparent rms thickness or radius of fluorescent spheres of 22, 55, and 100 nm in radii. Their average apparent sizes were measured at 0.15 μm, 0.15 μm, and 0.18 μm, respectively. These dimensions were obtained by fitting the function $g(y) = A \exp[-(y - \bar{y})^2/2\sigma^2] + By + C$, where A, B, C, $\bar{y}$, and σ are free parameters, to the intensity profile given by the two-dimensional sphere image summed over the 1-direction. The term $By + C$ captures the background level and slope variations due to slight inhomogeneities in the illumination, leaving σ as the rms apparent thickness. Parameters A and $\bar{y}$ are disregarded. As evidenced by these fits, both spheres and

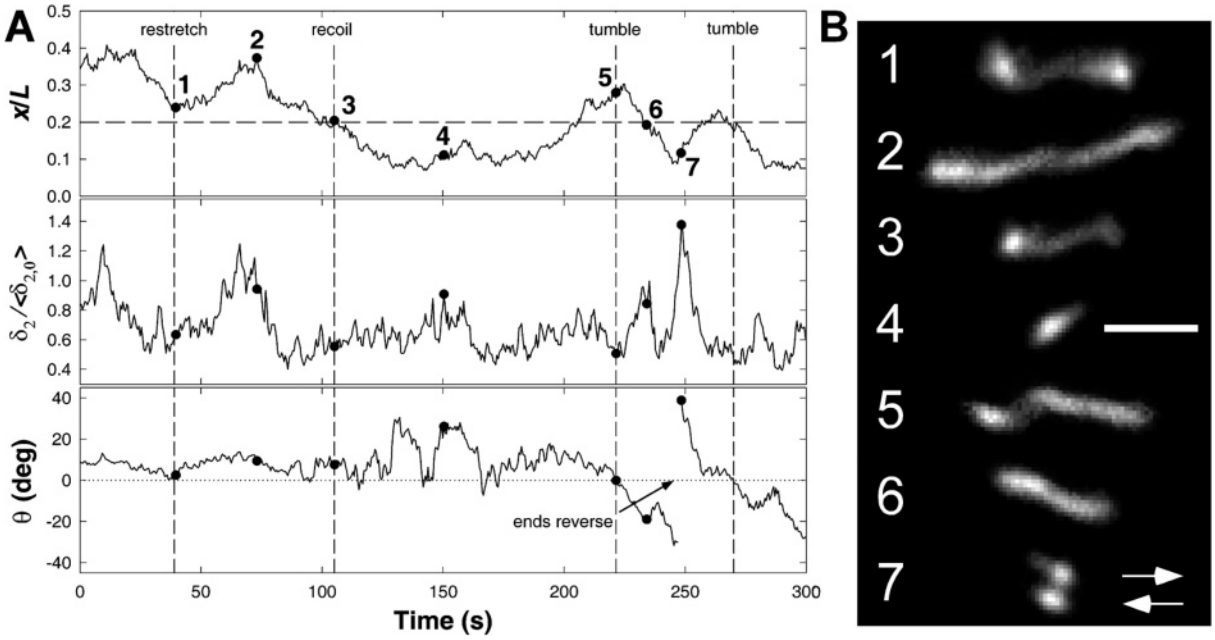

Figure 4. (A) Time traces of *extension*, *thickness* and *orientation*. The black circles, enumerated 1 thru 7 in the top plot, correspond to the images in part B. Vertical dashed lines show when the polymer went through a restretch, recoil and tumbles. The upper horizontal dashed line represents the highest extension observed in zero shear, $x/L \approx 0.2$, while the lower dotted line marks $\theta = 0$, for clarity. The orientation measure ranges from $-45°$ to $45°$ and changes sign when the polymer ends pass over each other, reversing their positions. (B) Series-in-time of 22 μm (λ-phage) DNA images in the flow-gradient plane. The horizontal white bar next to image no. 4 measures 3 μm and the arrows at the bottom show the direction of shear. The shear strength was $Wi = 6.1$.

polymers under flow assume approximately Gaussian shapes, while the resolution function is also Gaussian (for our level of precision). Hence the convolution gives for the rms size (δ): $\delta_{\text{apparent}}^2 = \delta_{\text{real}}^2 + \delta_{\text{resolution}}^2$. Using this formula, all three spheres yield $\delta_{\text{resolution}} = 0.14-0.15$ μm.

Before we deconvoluted the apparent thickness the effect of focusing errors was also taken into account. During each experiment it was necessary to continuously focus the molecule of interest to keep it from drifting out of the focal plane. Small fluctuations of the center-of-mass relative to the focal plane were found to impart significant increases in thickness. To minimize these variations, we revisited our data and eliminated out of focus images, as evidenced by its lack of sharpness. Through care and practice, we were able to recognize out of focus drifts corresponding to no more than a 10% increase in thickness. Since focusing errors also impart positive biases that are in principle nonuniform and most sensitive for thin conformations, this effect was factored into an effective $\delta_{\text{res+focus}} = (1.1)\delta_{\text{res}} = 0.16$ μm. Thus, we deconvolute the real polymer thickness and G_{22}, with $\delta_2 = \sqrt{\delta_{2,\text{apparent}}^2 - (0.16\mu\text{m})^2}$. Figure 3 illustrates the effect of this correction on the raw δ_2 data from our single polymer measurements and compares it to a Brownian dynamics simulation result[38] at the same shear strength of $Wi = 73$. The influence of resolution, as well as focusing errors, did not affect appreciably the polymer extension, orientation, or the individual G_{11} and G_{12} elements.

Results and Discussion

The direct visualization of polymer conformation in the flow-gradient plane provides a direct test of molecular theories and single-chain computer simulations (e.g., Brownian dynamics), as well as light scattering, neutron scattering and birefringence studies.

Polymers stretched after the onset of shear flow, acquiring initially steep positive orientations, and then slowly rotated and aligned with the flow direction. About 40−50% of alignments, depending on the Wi, were followed by end-over-end tumbling (negative orientations). This comprises the first experimental observation of tumbling in dilute polymer solutions, a phenomenon first hypothesized by Lumley[22] and later found in several Brownian dynamics[25−28,36,39−44] and Monte Carlo[45,46] simulation studies. In other cases the onset of tumbling was delayed by a restretch after a rotation back into a positive orientation. A plethora of conformations were visible in the flow-gradient plane during shearing (Figure 4B). They varied between highly stretched to globular and could not be easily organized into a few categories. Nevertheless a few qualitative generalizations can be made. For all shear strengths (Wi values), dumbbell and half-dumbbell shapes were commonly formed as the chain stretched right after a tumble or from a globular, or coiled, starting state. Folded conformations became frequent for $Wi \geq 10$. Movies of polymer motion in shear are available as Supporting Information.

For any given Wi value and contour length studied, we superimposed all recorded polymer images along their center-of-masses to obtain an ensemble-average of all conformations as shown in Figure 5. We found that polymers under shear flow adopt, on average, a cigar-shaped or approximately elliptical configuration projected onto the flow-gradient plane that is slightly tilted in a positive orientation. Such average configurations, while isotropic in a stagnant fluid, become highly anisotropic at high values of Wi. For instance, the ratio between semimajor and semiminor axes at $Wi = 292$ is approximately 10.

The mean fractional extensions (Figure 6A) ($\langle x \rangle/L$, where L is the contour length and $\langle\ \rangle$ denotes averaging) obtained here are in good agreement with the previous results by Smith et al.[23] In the present work, we have extended the upper bound of shear strength to $Wi = 584$. Even at this flow strength, $\langle x \rangle/L$ was less than, but still approaching ~0.5. We normalized our mean thickness measurements, $\langle \delta_2 \rangle$, with the ensemble-averaged equilibrium thickness, $\langle \delta_{2,0} \rangle$. The equilibrium radius of gyration was calculated as $R_G \approx \sqrt{3}\ \langle \delta_{2,0} \rangle$ and we

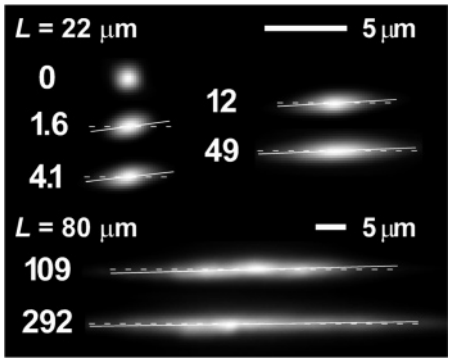

Figure 5. Average conformation of polymers in shear. For each *Wi*, all recorded images were superimposed at their center-of mass positions and equalized to span all gray levels. Numbers on the left of the images are *Wi* values. Length scales for both polymer sizes are given. Horizontal white dash lines indicate the flow direction while the solid ones show the average conformation orientation.

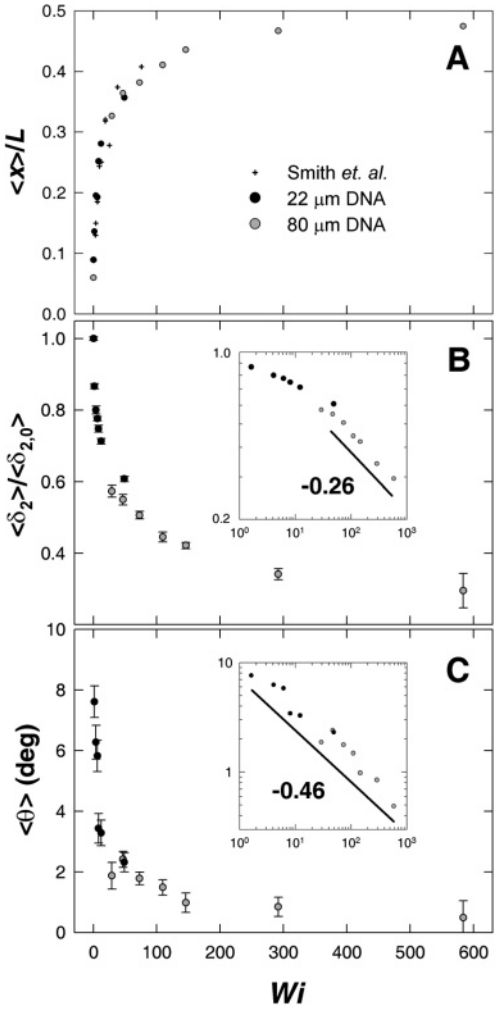

Figure 6. Measurements of ~10 molecules and 260−1300 strains per *Wi* averaged together. (A) Mean fractional extensions of both 22 μm DNA (black circles) and 80 μm DNA (gray circles) are plotted along with the results from Smith et al.[23] (crosshairs). (B and C) Mean polymer thickness and orientation at each *Wi*. Thicknesses were normalized with the equilibrium thickness, $\langle\delta_{2,0}\rangle$.

obtained $R_G = 0.65 \pm 0.02$ and 1.37 ± 0.05 μm for the 22 and 80 μm DNA pieces, respectively. These measurements agree with the $L^{0.61}$ scaling established previously for flexible double-stranded DNA.[47] Unlike the mean fractional extension, the mean fractional thickness curves did not appear to asymptote in the range of flow strengths studied (Figure 6B). The lack of overlap between the 22 and 80 μm DNA trends, while apparent, falls within the uncertainty of the resolution and focusing corrections, as well as the equilibrium averages used to normalize the average thicknesses.

On average, chains became not only thinner but also more closely aligned with the flow direction (Figure 6C) as the shear rate increased. The decays have power-law functionality and for the mean fractional thickness we obtained $Wi^{-0.26\pm0.02}$ for high *Wi* values, or $Wi > 40$ (inset of Figure 6B). This result supports theoretical predictions from both the Kramers bead−rod (BR) chain and wormlike chain (WLC) simulations with and without hydrodynamic interactions (HI).[26,27,48] The orientation angle was found to obey $\langle\theta\rangle \propto Wi^{-0.46\pm0.04}$ (inset of Figure 6C), and this behavior appeared to be uniform throughout the entire *Wi* range. Thanks to our single-molecule approach, combined with long polymer time scales and good flow stability, we were able to measure both thickness and orientation decays at high enough *Wi* to reveal the aligning behavior at large shear strengths, beyond what has been possible with light scattering ($Wi < 10-20$)[5−8] and birefringence techniques ($Wi < 1$).[9]

The ability to observe polymers directly enables us to extract from each image the instantaneous conformational moments that underlie bulk non-Newtonian fluid properties. In the present study, where projections onto the flow-gradient plane are visible, moments of the conformation which are related to the polymer shear viscosity and the first normal stress coefficient become accessible. If hydrodynamic interactions (HI) between chain segments are negligible, then one can write these two quantities in terms of single-molecule parameters by employing the Giesekus stress tensor formula.[27] The Giesekus expression for a polymer discretized into *N* Kuhn steps in a steady shear flow has the form:

$$\tau_{ij}^{p} \propto Wi \sum_{v=1}^{N} \langle \delta_{i1} R_2^{v} R_j^{v} + \delta_{j1} R_i^{v} R_2^{v} \rangle$$

where τ_{ij}^{p} is the stress tensor due to an ensemble of polymers, δ_{ij} is the Kronecker delta, and R_i^{v} is the distance of step v from the center-of-mass in the ith direction. The dimensional constant of proportionality involves the Kuhn step diffusion time and the overall relaxation time of the chain. This expression, although convenient, neglects HI and other intramolecular interactions. Nevertheless, simulations by Jendrejack et al. suggest that a consideration of HI and excluded volume (EV) produces a negligible change in the scaling properties of these stress coefficients for even longer (126 μm) DNA polymers than the ones in this study, for which HI presumably exerts a greater influence. A detailed study comparing experimental results from shear flow measurements of λ-phage DNA to WLC DNA models with similar parameters was recently completed.[38] In that work, HI/EV forces were both included and excluded (free-draining) in those models, and they were found to reproduce faithfully our single molecule data over the entire range of *Wi* investigated. The polymer contribution to the shear viscosity and first

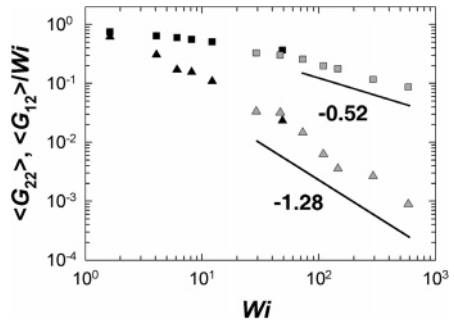

Figure 7. Polymer contributions to the shear viscosity ($\langle G_{22}\rangle$, squares) and the first normal stress coefficient ($\langle G_{12}\rangle/Wi$, triangles) measured directly from the conformations of single polymers and then averaged for 22 μm DNA (black symbols) and 80 μm DNA (gray symbols). The Giesekus stress tensor expression was utilized to write the desired stress coefficients in terms of the known radius of gyration tensor elements. Both quantities were normalized to unity at zero shear rates. The black lines depict the power-law fitted exponents over the fastest decaying portion of the curve in the high shear region.

normalstress coefficient are defined, respectively, as

$$\eta^{\mathrm{p}} = \frac{{\tau_{12}}^{\mathrm{p}}}{\dot{\gamma}} \quad \text{and} \quad {\Psi_1}^{\mathrm{p}} = \frac{{\tau_{11}}^{\mathrm{p}} - {\tau_{22}}^{\mathrm{p}}}{\dot{\gamma}^2}$$

After substituting in the appropriate expressions for the ${\tau_{ij}}^p$ tensorial elements, we arrive at the desired proportionality relationship written in terms of the known radius of gyration tensor elements

$$\eta^{\mathrm{p}} \propto \frac{\langle G_{22}\rangle}{2} \quad \text{and} \quad {\Psi_1}^{\mathrm{p}} \propto \frac{\langle G_{12}\rangle}{Wi}$$

Interpreted in this way, i.e., within the Giesekus expression, the shear viscosity curve shows a high shear rate ($Wi > 70$) decay exponent of $\eta^{\mathrm{p}} \propto Wi^{-0.52}$ (Figure 7). This compares favorably with the $\sim Wi^{-1/2}$ dependence found in bulk rheometry of not only λ-phage DNA[28] but also a wide variety of dilute synthetic polymer−solvent systems.[3,49] Also, interpreted within the Giesekus expression, the first normal stress coefficient was found to decrease as ${\Psi_1}^P \propto Wi^{-1.28}$ over the entire range studied (Figure 7). Brownian dynamics simulations on both Kramers bead−rod chains[25,27,28] and WLC[48] with and without HI and excluded volume (EV) forces have been used to examine these stress components and the predicted thinning exponents are in excellent agreement with our single molecule data. By rheometry, normal stress decays are difficult to quantify since in dilute solutions they are typically an order of magnitude smaller than shear stresses. In addition, the inherent polydispersity of synthetic polymer systems in many of these studies may have broadened the transition from the low Wi plateau to the thinning regime.[50] Consequently, there is no accepted value for the normal stress thinning exponent in the rheometry literature.

Probability distributions of extension, configuration thickness, and orientation are plotted in Figure 8, parts A, B and C, respectively. Extension distributions in Figure 8A corroborate previous findings[23] while showing that for a much higher flow strength and longer polymer (compared to $Wi = 76$ of ref 23) the distribution is still broad and approximately flat but with shallower drop-offs at both ends that extend up to 90% of its contour length. Both parts B and C of Figure 8 indicate a gradual polymer confinement in gradient and orientation space: increasingly stronger flows quickly advect, and later realign, any thickening fluctuations (i.e., increases in δ_2) created by Brownian motion. An equivalent description invokes a balance between Brownian motion, which forces the conformation to randomize, against flow forces, which aligns chain segments. The end result is a confinement in the gradient of shear direction, and concurrently an increase in chain extension and alignment with the flow direction, as the polymer is forced to explore thinner conformations, where the relative velocity across the chain is smaller.

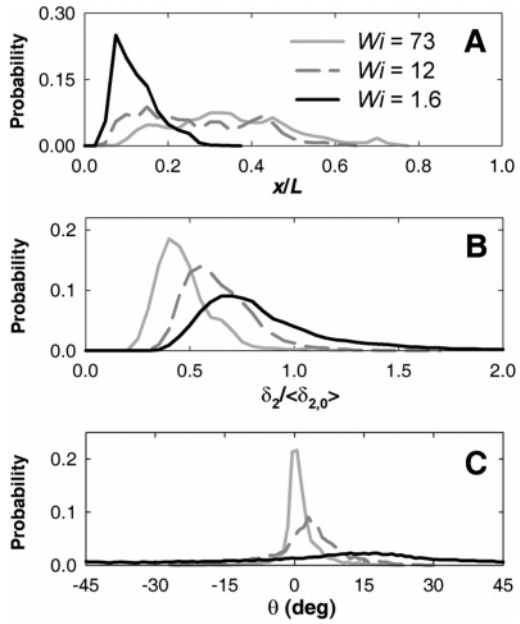

Figure 8. Probability distributions of (A) extension, (B) thickness, and (C) orientation. Both 22 μm DNA ($Wi = 1.6$ and 12) and 80 μm DNA ($Wi = 73$) are shown. The bin sizes are 0.025, 0.05, and 1°, respectively. Instances where a molecule adopted a globular conformation and no preferred orientation could be assigned was rare (< 2%) for $Wi = 1.6$ and absent for higher flows. Probabilities were normalized by the total number of data points (~500−21000).

We recall that positive angles were measured from the flow direction toward the opposite sense of rotation of the vortical component of the applied shear flow. Hence, at positive orientations the flow attempts to stretch the polymer against its entropic elasticity. Because this is a slow process, polymers dwell longer at positive than negative orientations. This is observed in all nonzero shear rate orientation probabilities. However, upon closer inspection of these probability distributions we found that the area under the positive orientation region was ~0.75 of the total area for all probed Wi numbers greater than zero, $1.6 \leq Wi \leq 584$ (Figure 9). Here, we recast the total probabilities in terms of fractional dwell times at positive orientations, $t_+/(t_+ + t_-)$. A linear fit through the data reveals a slope of $-3 \times 10^{-5} \pm 10^{-4}$. At equilibrium with $Wi = 0$ the fractional time spent at either orientation state was ~ 0.5, as expected from an ensemble-averaged isotropic conformation (see Figure 5). The fractional time was also insensitive to an almost 4-fold change in contour length.

The constant fractional time of positive and negative orientation states strikes a resemblance with the dynamical behavior of rigid ellipsoids of revolution in shear flow. The fractional dwell times of rigid ellipsoids are, according to Jeffery's treatment,[51−53] also invariant with

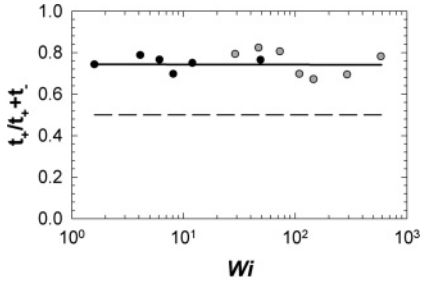

Figure 9. Fractional dwell times of positive orientation conformations for 22 μm DNA (black circles) and 80 μm DNA (gray circles). The fitted line has a mean = ~0.75 and slope = $-3 \times 10^{-5} \pm 10^{-4}$ over more than two decades of *Wi* and two polymer lengths. The dashed line represents schematically the rigid ellipsoid behavior over a range of equivalent shear strengths.

respect to both shear rate and particle size (as long as they are non-Brownian). The similarity is perhaps unexpected because polymers are highly flexible objects with many internal modes and subject to Brownian motion. Nevertheless one important difference remains. The angular velocities of rigid ellipsoids are symmetric with respect to the flow axis. In other words, they spend equal times at either positive or negative orientations, or $t_+/(t_+ + t_-) = 0.5$. Polymers are weighted toward positive orientations. We regard this difference as a consequence of the polymer's entropic elasticity due to its flexibility.

Note in this context that the relative probability of flexible polymer orientations in high *Wi* shear flows have been examined in the past through the Hookean model[42] with the finding that

$$\frac{t^+}{t^+ + t^-} = 2P_{\mathrm{I}} = \frac{1}{2} + \frac{1}{\pi}\tan^{-1}\left(\frac{Wi}{\sqrt{1+Wi^2}}\right)$$

where P_{I} is the cumulative probability of a bead of the dumbbell model lying in the first quadrant. In the limit as $Wi \to \infty$ this gives identically $t^+/t^+ + t^- \to {}^3/_4$. Thus, in this regard, our measurements suggest that the DNA is dynamically acting as a linear dumbbell. Further ramifications of this result are examined when directly comparing our experimental findings to WLC bead–spring Brownian dynamics simulations.[47]

To further examine the dynamics of DNA in shear flow, we have classified shear-induced motions into three categories. As a starting point, a chain becomes stretched and aligned as shown schematically in Figure 10A. Once in this state, the chain will start to recoil since the net shearing force is not enough to overcome its entropic restoring force. From this point, we observe three possibilities: (i) a Brownian fluctuation can tip the chain to a more positive angle where the shear flow will extend it again (restretch), (ii) the chain will orient nearly parallel to the shear flow and fully relax due to entropy (recoil), or (iii) the chain will tumble into a negative angle, where the shear flow causes a rapid compaction resulting in one polymer end moving over the other, thus reversing their positions (tumble).

Using this classification scheme, recoil, restretch, and tumbling events were counted by inspection of the movies. Then, the percentage distribution of each event was calculated by dividing the event count by the total number of captured events. The results are plotted in Figure 10B. Here, we were restricted to the 22 μm DNA data since for the larger polymer at higher *Wi* values

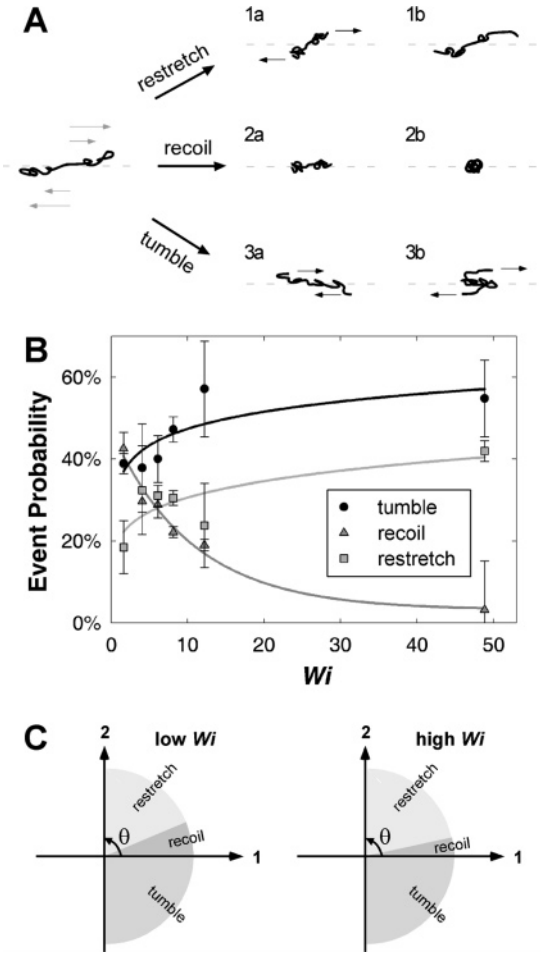

Figure 10. (A) Schematic depiction of the three observed dynamical events. (B) Depiction where each event type was counted by careful inspection to obtain percentage distributions for all *Wi* values probed with the 22 μm (λ-phage) DNA piece. Error bars were obtained by counting instances where classification was unclear due to spatial and temporal resolution limitations. Lines are meant only as guides. (C) Drawing showing where in orientation space the observed dynamical events are most likely to occur and showing the narrowing of the recoil region under increasing *Wi* values.

too few recoiling events were captured to produce significant figures. At the slowest shear rate or $Wi = 1.6$ recoiling was very common while restretching was rare. The opposite occurred as *Wi* increased. From our observations it was apparent that for high enough *Wi* even the smallest Brownian perturbation caused chain segments to sample a shear strong enough to cause a restretch. However, at low *Wi*, Brownian fluctuations had to be rather large to create a restretch, and so they had a low probability of occurrence, making recoiling prevalent over restretching. We envision the above description as three partitions in orientation space, each dominated by one of the three outcomes (Figure 10C). Steep orientation angles are prevalent in restretching events, while tumbling takes place when the orientation is negative. The region between the two is dominated by recoiling. In the limit where $Wi \to \infty$, we expect the recoil region to vanish, and so an extended chain in perfect alignment has an equal probability of receiving a Brownian "kick" in either direction, leading to a restretch or a tumble. This proposition is consistent with the trend in our data.

The dynamical interplay between the flow and gradient dimensions was characterized by cross-correlating

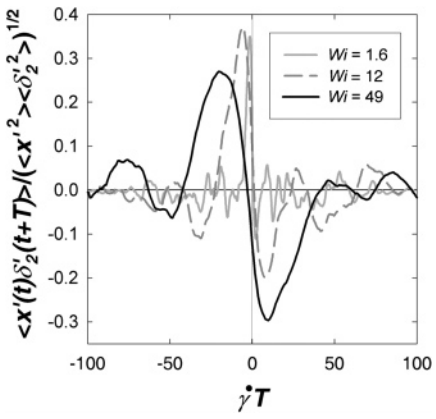

Figure 11. Cross-correlations between extension and thickness for each molecule were averaged together and normalized such that a perfect correlation equaled unity. Mean-subtracted time trajectories were used in the computation. The horizontal axis is dimensionless lag or strain.

chain extension and thickness fluctuations over time. The cross-correlation is defined as

$$C_{x\delta}(T) = \langle x'(t)\delta_2'(t+T)\rangle / \sqrt{\langle x'^2(t)\rangle\langle \delta_2'^2(t)\rangle}$$

where primed variables indicate fluctuating or mean-subtracted quantities. Averages were taken over all molecules at a particular *Wi*. The results are plotted vs dimensionless lag or strain (Figure 11). As we move away from zero strain, we encounter large peaks at negative strain lags and valleys at positive. The large peaks represent the average tendency of changes in extension to follow the thickness in the same sense, such as when thickening of the polymer led to stretch at some strain value later and, equivalently, when thinning caused a collapse of extension. Conversely, thickness changes followed extension changes in the opposite sense, as signaled by the valleys at positive lag. This corresponds to both the thinning motion after a stretch, and the thickening tendency as the polymer crumples. Corroborated by our own visual observations we conclude that, on average, extension and thickness fluctuations are coupled in a causal chain relationship producing a repeating thickening−stretching−thinning−crumpling cycle.

As pointed out by Woo et al.,[36] valleys are absent in the analytical solution of either a Hookean dumbbell or a Rouse chain, both of which have linear springs, but appear with the inclusion of nonlinear, finitely extensible spring forces. For a Hookean dumbbell the force acting along the gradient direction is simply $F_2^{spr} = HR_2$, where H is the spring constant and R_2 is the gradient thickness of the dumbbell. Therefore, the aligning force (the "2"-direction force) is independent of extension (R_1). That is, conformational changes in the flow and gradient directions are uncoupled in linear models. Hence, neither the stretching phase implies a subsequent aligning motion nor does the collapse of extension, for instance via recoiling, cause the polymer to become thicker. In finite contour length chains all dimensions are coupled by their maximum extensibility, and the valleys present in our data validates this assertion. Furthermore, under stronger shearing currents, instances of a high degree of stretch had visibly more rapid and pronounced subsequent aligning motions. That is, the coupling between thickness and extension became stronger due to the nonlinear nature of the spring force. This is demonstrated as a deepening of the valleys under an increasing shear rate.

Cross-correlations alone cannot resolve which mechanism or mechanisms give rise to the observed oscillations. As pointed out before, restretch, recoil and tumble events were all visually identified as different modes of length-fluctuations. To clarify this issue, we compared the cross-correlation oscillations with the restretch, recoil and tumble frequencies obtained by direct inspection of the recorded movies. To extract the frequency of oscillation from the cross-correlation curves we measured the strain separation between the largest peak and valley (close to zero strain) as a half-oscillation, or $\Delta\gamma$. These values were converted to dimensionless oscillation frequencies via $f_{osci}\tau = Wi/2\Delta\gamma$. The oscillation frequencies were $f_{osci}\tau \approx 0.1$, 0.3, and 0.6 for $Wi = 1.6$, 12 and 49, respectively.

To obtain all event frequencies we divided the event count by the total length of duration of the experiment for each *Wi* value. The frequencies were then also made dimensionless with the inverse longest polymer relaxation time, $1/\tau$. The resulting plot is shown for the tumbling frequency, f_{tumb}, in Figure 12A along with an inset showing a blow-up for the 22 μm DNA data only with the restretch and recoil frequencies as well. The tumbling frequency grew like $Wi^{0.62}$ over the entire *Wi* range. The agreement between the cross-correlations and only the tumbling frequency suggests that large-scale (comparable to the contour length) polymer conformation fluctuations in shear evolve and oscillate with a monotonically increasing, flow-dependent characteristic frequency, which is approximately the tumbling frequency. These observations will be investigated in detail in another paper.[54] From our subjective observations, restretching events are typically small fluctuations that contribute only small delays to the average cycle. Recoiling, on the other hand, while having significant motion amplitudes, were rare events for all but the lowest shear rates.

The tumbling process is then the mechanism by which the chain cyclically absorbs and releases energy from and to the surrounding fluid. The graph in Figure 12A indicates that the tumbling frequency increases monotonically with shear strength for at least the range of *Wi* values studied. Also, values for the 80 μm DNA do not overlap with the 22 μm DNA set, but fall slightly below it. We developed a physical description of these findings by deriving a tumbling frequency equation from simple advection and diffusion concepts applied to flexible chains.

We dissected the tumbling process into four distinct phases: stretching, aligning, flipping and collapsing. A schematic representation of a dumbbell undergoing all four phases is shown in Figure 13. This partition scheme was motivated by our observations of polymer motion while having the concomitant benefit of separating advection-dominated from diffusion-dominated phases, thus facilitating a mathematical treatment. In advection-dominated motion we expect the polymer to be mostly "dragged along" hydrodynamically by the shear flow motions of the surrounding solvent molecules; whereas in diffusion-dominated phases Brownian motion becomes the major driving force. It is important to mention that in this derivation the recoil and restretch events are neglected. Again, this neglect is supported by an approximate match between peak and valley separation in the cross-correlations with the tumbling

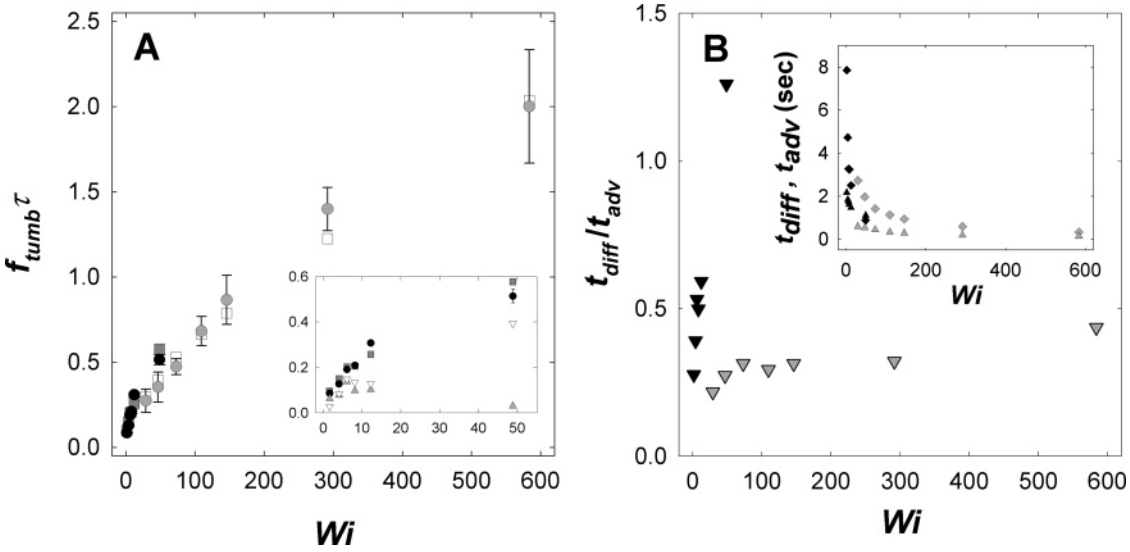

Figure 12. (A) Tumbling frequencies obtained by counting clear, end-over-end tumbling events for 22 μm (black circles) and 80 μm (gray circles) and made dimensionless with $1/\tau$. Overplotted are the values from the tumbling frequency equation for 22 μm (gray squares) and 80 μm (white squares). Error bars were estimated as τ/t_{tot}, where t_{tot} is the total duration of the experiment at a particular *Wi* value. The inset plots $f_{event}\tau$ for the tumbling, as well as the restretch (inverted white triangles) and recoil (gray triangles) frequencies for the 22 μm DNA data only. There are no fitted parameters for the theoretical values. (B) Ratio of advection to diffusion time scales, t_{adv}/t_{diff}. As before, the black symbols represent 22 μm DNA data while the gray symbols are 80 μm DNA data. The inset plots the absolute times of advection (diamonds) and diffusion (triangles) in seconds.

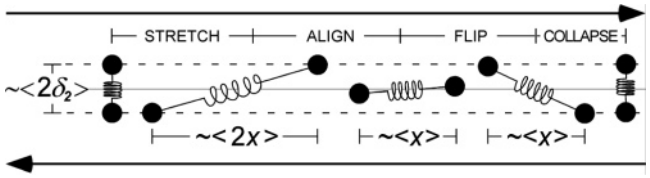

Figure 13. Schematic depiction of a dumbbell undergoing the four phases of motion in a tumbling cycle. The solid gray line represents the stagnation plane (zero flow). Characteristic dimensions are also shown.

frequency. Nevertheless, it may introduce some error that will be examined in more detail in our subsequent paper.[46]

On occasion, we will refer to the simplest polymer model, the dumbbell model, for the sake of clarity while the derivation remains general enough for fine-grained models. The equation we seek is of the following form:

$$f_{\text{tumb}}\tau = \frac{\tau}{t_{\text{stretch}} + t_{\text{align}} + t_{\text{flip}} + t_{\text{collapse}}}$$

Here t is the time duration of each phase. We now proceed to find the appropriate expressions for each term.

During the stretching phase, we assume the polymer stretches a distance of approximately twice the average extension, $\sim 2\langle x\rangle$. This assumption is well-justified by our own observations. For instance, the mean fractional extensions at $Wi = 1.6$, 12, and 292 (Figure 6A) are 0.14, 0.28, and 0.47, respectively. The maximum extensions, which occur at the end of the stretch phase can be readily determined from the extension histograms (Figure 8A), to be 0.3, 0.6, and 0.9, respectively. This observation is also consistent with the apparent $\sim$0.5 asymptote of the mean fractional extension at high *Wi* since the maximum stretch is 1.0. The stretching speed of a dumbbell is $\sim 2\dot{\gamma}\langle R_2\rangle$, where R_2 is the distance of a polymer segment from the center-of-mass in the gradient direction, thus making $2R_2$ the interbead separation in the same direction. Here, we have neglected the effect of the polymer's entropic elasticity to resist deformation, thus making polymer and fluid velocities identical. In other words, motion is assumed to be *affine*. We delay the consideration of polymer entropic forces (and therefore *nonaffine* motion) into our derivation until the moment the polymer extends to the point where its total entropic restoring force grows enough to approximately balance the net hydrodynamic drag, thus halting the stretch. At this point the stretching ends and the aligning phase begins. For now, we convert R_2 to the experimentally measured δ_2 by making use of its definition for a dumbbell ($N = 2$):

$$\delta_2 = \sqrt{\frac{1}{N}\sum_{\nu=1}^{N}(R_2^{\nu}R_2^{\nu})} = R_2$$

The duration of the stretching phase then becomes

$$t_{\text{stretch}} = \frac{\langle x\rangle}{\dot{\gamma}\langle\delta_2\rangle}$$

As stated before, the aligning phase begins when the spring force balances the drag force: $F^{\text{spring}} \approx F^{\text{drag}}$. The polymer aligns a distance $\sim\langle\delta_2\rangle$, with a speed $\varsigma^{-1}F_2{}^{\text{spring}}$. To make the expression tractable we substitute $F^{\text{spring}} \approx F^{\text{drag}} = \varsigma\dot{\gamma}\langle\delta_2\rangle$. Also, at the beginning of the alignment phase angles are small (for $Wi > 1$). For instance, we estimate that at $Wi = 1.6$ the orientation angle in question is at most $\sim 4°$ and decreases for higher *Wi*. This allows the substitution $\sin\theta \approx \tan\theta = \langle\delta_2\rangle/\langle x\rangle$ without loosing accuracy. We are then able to write the approximate speed of alignment using known variables:

$$\varsigma^{-1}F_2{}^{\text{spring}} \approx \frac{\dot{\gamma}\langle\delta_2\rangle^2}{\langle x\rangle}$$

Thus, the time for alignment is identical to that of the stretch

$$t_{\text{align}} = \frac{\langle x \rangle}{\dot{\gamma}\langle \delta_2 \rangle}$$

As the polymer's orientation approaches full alignment ($\theta = 0$), net shearing forces acting across the polymer nearly vanish, thus making the flipping process predominantly diffusive. For a flip in polymer orientation to later result in a clear end-over-end tumble, the fluctuation has to be statistically significant, that is, at least one standard deviation of the conformation in the direction of motion, or $\sim\langle \delta_2 \rangle$. The flipping time is then $t_{\text{flip}} \sim \langle \delta_2^2 \rangle / D(\delta_2)$ where the gradient diffusivity of a piece of the chain, as pointed out by Doyle et al.,[27] is itself a function of the gradient dimension. He found that $D(\bar{\delta}_2) = \bar{\delta}_2^{-2/3}$, where $\bar{\delta}_2$ is the dimensionless thickness, by measuring the bead self-diffusivity of a chain relaxing via Brownian dynamics simulations of a Kramers BR chain. In this equation, the diffusivity was made dimensionless with a length a, the Kuhn step length, and a time $t_s = \varsigma^{\text{eff}} a^2$, where ς^{eff} is its corresponding drag coefficient normalized by kT. A somewhat smaller exponent was proposed by Hur et al.[26] $D(\bar{\delta}_2) = \bar{\delta}_2^{-1}$. In this alternative argument, a bead must drag at least an order $\bar{\delta}_2$ nearest neighbors to move along the gradient direction. Here we have considered both approaches and found a somewhat better agreement with the former exponent. With that, the flipping term written in dimensional form becomes

$$t_{\text{flip}} = t_s \left(\frac{\langle \delta_2 \rangle}{a} \right)^{8/3}$$

During the aligning phase the net shearing forces across the conformation weaken and as a result the polymer partially retracts. In addition, further relaxation occurs while the polymer is diffusing toward a negative orientation in the flipping phase. At this point, the beginning of the collapse, the molecule is found roughly halfway between the point of highest stretch of $\sim 2\langle x \rangle$ at the beginning of the alignment phase and a negligible extension, by comparison, at the end of the collapse. Hence, we take the relative distance the polymer has to collapse to reach the beginning of the next cycle to be the average extension, or $\sim\langle x \rangle$. Like the stretching phase, the collapse is also assumed to be affine, and so the speed is also $\sim 2\dot{\gamma}\langle \delta_2 \rangle$. The collapsing time is then one-half either the stretching or aligning time:

$$t_{\text{collapse}} = \frac{\langle x \rangle}{2\dot{\gamma}\langle \delta_2 \rangle}$$

The final equation for the tumbling frequency made dimensionless with $1/\tau$ is then

$$f_{\text{tumb}}\tau = \left[\frac{5}{2} \frac{\langle x \rangle}{Wi\langle \delta_2 \rangle} + \frac{t_s}{\tau} \left(\frac{\langle \delta_2 \rangle}{a} \right)^{8/3} \right]^{-1}$$

We tested the tumbling frequency equation by using $a = 2(66\text{ nm}) = 0.132\ \mu\text{m}$ for the Khun length of our stained DNA and $\tau = 28$ and 251 s for the 22 μm and 80 μm DNA sizes, respectively. The time scale, t_s, could not be measured directly with the current experimental approach. Instead we used simulation data and linearly extrapolated it for our solvent viscosity of 300 cP. Hur et al.[26] cites $t_s = 0.033$ s for a FD WLC model of λ-phage DNA ($\sim$ 22 μm) with a longest relaxation time of $\tau =$ 0.9 s. This time scale becomes $t_s = 1.2$ s for our solvent. This value depends only on the solvent viscosity and solvent/polymer chemistry but not on its contour length; hence, the same value was used for the longer DNA piece. The results are shown alongside with the data in Figure 12A. Even though good agreement was found without the need for a fitting parameter, several approximations where made in the course of this derivation including the neglect of restretch and recoil motions and the introduction of ad hoc quantities for the stretch and collapse distances. Data on different polymer molecular weights and chemistries would be required to test the generality of our equation.

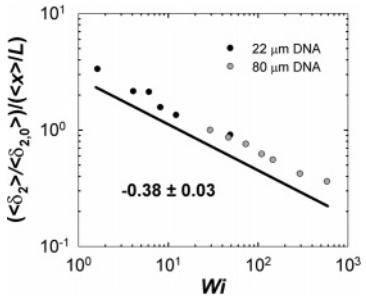

Figure 14. Ratio of mean fractional thickness to mean fractional extension in shear flow appears to obey a single exponent power-law decay throughout more than two decades in Wi and two different contour lengths ($R^2 = 0.98$). Black circles represent 22 μm DNA, and gray circles are 80 μm DNA ensemble averages.

Nevertheless, the success of our theory in reproducing single molecule data encourages us to further explore the relative importance of advection vs diffusion processes in the tumbling cycle. To accomplish this we sort each term in the tumbling frequency equation as an advective or diffusive process. The stretch, align and collapse phases scale with the shear rate, so these phases are predominantly influenced by flow advection:

$$t_{\text{adv}} = \frac{5}{2} \frac{\langle x \rangle}{Wi\langle \delta_2 \rangle}$$

Similarly the flipping phase is the only predominantly diffusive process:

$$t_{\text{diff}} = \frac{t_s}{\tau} \left(\frac{\langle \delta_2 \rangle}{a} \right)^{8/3}$$

In Figure 12B, we plotted the ratio of the diffusion to advection times and in its inset the diffusion and advection times separately. Both terms display a rapid decay with increasing Wi and a significant change with polymer size. Here, it becomes apparent that for most of the range of Wi values and both polymer lengths tumbling was rate limited by flow advection or shear rate. Conversely, diffusion became rate limiting around $Wi > 49$ for the 22 μm DNA only.

Next, we derived the scaling laws for advection and diffusion times with respect to Wi and L to understand the trends in the $t_{\text{diff}}/t_{\text{adv}}$ ratio. We employed $\tau \propto L^{1.7}$ for the longest relaxation time of DNA.[32] For the thickness scaling with the contour length we used the $\langle \delta_2 \rangle \propto L^{0.65}$ result from Woo et al.,[42] extracted from nonequilibrium Brownian dynamics simulations without HI. Also, from the present study we know that $\langle \delta_2 \rangle \propto Wi^{-0.26}$, $\langle x \rangle \propto L$ and $\langle \delta_2 \rangle / \langle x \rangle \propto Wi^{-0.38}$ (see Figure 14). This latter result is consistent with the Graetz−Levecque layer argument

proposed in a previous paper.[26] Together, they yield the following approximate relations:

$$t_{adv} \propto Wi^{-0.62}L^{0.35} \quad \text{and} \quad t_{diff} \propto Wi^{-0.66}L^{0.0} \qquad \text{for } (Wi \gg 1)$$

It is perhaps not surprising that both the advection and diffusion times should display nearly the same shear rate dependency since polymers shrink their average gradient dimension in order to keep a balance between flow and Brownian time scales. As for the contour length dependence, the advection time grows moderately while the diffusion time presents little or no change. The ratio of both terms scales as

$$\frac{t_{diff}}{t_{adv}} = \frac{2}{5}Pe\left(\frac{\langle\delta_2\rangle}{a}\right)^{8/3}\frac{\langle\delta_2\rangle}{\langle x\rangle} \propto Wi^0L^{-0.4}$$

where the Peclet number has the usual definition: $Pe = \dot{\gamma}t_s$. The contour length dependency suggests, for instance, that longer polymers have a more prolonged influence by advection over diffusion, thus implying that longer polymers tumble more deterministically.

The tumbling frequency equation should also be able to predict the constant fractional time at positive orientations observed previously. The stretch and align phases belong to positive orientations while the collapse occurs at negative orientations. The flipping time, however, must be partitioned at some proportion between the two orientation states and this proportion is not known a priori. As implied in the derivation, the end of the alignment phase and the beginning of the flipping phase is not well-defined in orientation space. That is, the transition occurs when Brownian forces overcome advection forces as the orientation approaches zero. Furthermore, the fraction of the flipping time assigned to either orientation may be itself a function of both Wi and L. In the case where the diffusion time is negligible compared to the advection time, $t_{adv} \gg t_{diff}$, our theory predicts

$$\frac{t_+}{t_+ - t_-} \approx \frac{t_{stretch} + t_{align}}{t_{collapse} + t_{stretch} + t_{align}} = 0.8$$

On the other hand, by assigning ~50−70% of the flipping time to positive orientations the time ratio could be kept at ~0.75 for in the entire Wi range. The emergent physical picture shows that polymers dwell more time at positive orientations thanks to the non-affine alignment motion after an affine stretch. Furthermore, since some relaxation of the stretched state occurs between the beginning of alignment and end of the flipping phase, the collapse phase is shortened, and this creates further bias toward the positive orientation state. Finally, since motion at both orientation states are equally affected by the shear flow advection, their relative times remain, on average, constant over a wide range of Wi, at least for advection-dominated tumbling cycles.

Conclusions

We have reported the first direct observation in the flow-gradient plane of individual, isolated polymers in a steady shear flow. By looking at single polymers we were able to provide a precise link between experimentation and molecular-level theories, while also measuring microscopically the behavior of bulk rheological properties. We found that while polymers display a wide variety of conformations in shear, on average the configuration space narrows in the gradient direction, as predicted by previous simulations and suggested by rheometric measurements. We have measured from individual polymer images the microscopic contributions to the radius of gyration tensor and calculated the power-law decays for both $\langle G_{22}\rangle \propto Wi^{-0.52}$, and $\langle G_{12}\rangle/Wi \propto Wi^{-1.28}$. The relation between bulk stresses and microscopic parameters made via the Giesekus stress tensor, which neglects HI and EV, gives decay exponents which support the predictions of stress calculation from Brownian dynamics simulations on both Kramers BR chains[25,27,28,44] and WLC[26,48] with and without HI and EV.

Our ability to resolve individual polymer chain dynamics revealed a splitting of the chain residence times into positive and negative orientation states. The fraction of time a polymer spends in positive orientations was ~0.75 and constant with respect to Wi from Wi ~1.6 to at least 584. This constant was also insensitive, to within error, to a 4-fold difference in contour length. This feature is identical to that for a Hookean dumbbell at high values of Wi and was compared and contrasted with Jeffery's analogous result for rigid ellipsoids.[51−53] Three modes of shear-induced stretching transitions were found: recoil, restretch, and tumble. Cross-correlations between thickness and extension fluctuations revealed a causal chain relationship leading to four phases of motion: thickening, stretching, thinning, and crumpling recoiling. Comparison between the observed tumbling frequencies and cross-correlation oscillations revealed that polymer conformations in shear evolve and oscillate with a characteristic frequency which is the tumbling frequency. Finally, we developed an approximate expression for the tumbling frequency using simple advection and diffusion concepts. Our derivation was able to quantitatively predict tumbling frequencies as well as explain the constant fractional dwell time at positive orientations. The equation was then analyzed to ascertain the rates of advection vs diffusion processes in the tumbling cycle, as well as to predict its contour length and Wi dependencies. One consequence revealed by our theory is that long polymers tumble at a rate limited by advection, while short polymers may become rate limited by diffusion instead and even loose its ability to tumble. The data and insights presented herein should prove useful in providing a more complete understanding of polymer flow physics.

Acknowledgment. The authors would like to thank M. Gallo and E. Chan at US Genomics for providing samples of the 185-kbp DNA. This work was supported, in part, by grants from the Materials Research Science and Engineering Center Program of the National Science Foundation (E.S.G.S.), the Air Force Office of Scientific Research, and the NSF (S.C.).

Supporting Information Available: Text giving a captions for movies S1−S4, describing the motion of DNA in various lengths. This material is available free of charge via the Internet at http://pubs.acs.org.

References and Notes

(1) Muller, S.; Larson, R.; Shaqfeh, E. *Rheol. Acta* **1989**, *28*, 499−503.
(2) Groisman, A.; Steinberg, V. *Nature (London)* **2000**, *405*, 53−55.

(3) Larson, R. *Constitutive Equations for Polymer Melts and Solutions*; Buttersworth: Stoneham, MA, 1988.
(4) Cottrell, F.; Merrill, E.; Smith, K. *J. Polym. Sci., Polym. Phys. Ed.* **1969**, *7*, 1415.
(5) Lindner, P.; Oberthur, R. *Colloid Polym. Sci.* **1988**, *266*, 886−897.
(6) Link, A.; Springer, J. *Macromolecules* **1993**, *26*, 464−471.
(7) Lee, E.; Solomon, M.; Muller, S. *Macromolecules* **1997**, *30*, 7313−7321.
(8) Li, L.; Larson, R. *Macromolecules* **2000**, *33*, 1411−1415.
(9) Bossart, J.; Ottinger, H. *Macromolecules* **1997**, *30*, 5527−5540.
(10) Fuller, G.; Leal, L. *Rheol. Acta* **1980**, *19*, 580−600.
(11) Kirkwood, J. *Recl. Trav. Chim. Pays Bas* **1949**, *68*, 649−660.
(12) Rouse, P. *J. Chem. Phys.* **1953**, *21*, 1272−1280.
(13) Zimm, B. *J. Chem. Phys.* **1956**, *24*, 269−278.
(14) Peterlin, A.; Heller, W.; Nakagaki, M. *J. Chem. Phys.* **1958**, *28*, 470−476.
(15) Warner, H. *Ind. Eng. Chem. Fundam.* **1972**, *11*, 379-&.
(16) deGennes, P. *J. Chem. Phys.* **1974**, *60*, 5030−5042.
(17) Hinch, E. *J. Fluid Mech.* **1976**, *75*, 765−775.
(18) Magda, J.; Larson, R.; Mackay, M. *J. Chem. Phys.* **1988**, *89*, 2504−2512.
(19) Wedgewood, L.; Ottinger, H. *J. Non-Newtonian Fluid Mech.* **1988**, *27*, 245−264.
(20) Wedgewood, L.; Ostrov, D.; Bird, R. *J. Non-Newtonian Fluid Mech.*, *40*, 119−139.
(21) Kuhn, W.; Kuhn, H. *Helv. Chim. Acta* **1943**, *26*, 1394.
(22) Lumley, J. *Annu. Rev. Fluid Mech.* **1969**, *1*, 367-&.
(23) Smith, D.; Babcock, H.; Chu, S. *Science* **1999**, *283*, 1724−1727.
(24) LeDuc, P.; Haber, C.; Bao, G.; Wirtz, D. *Nature (London)* **1999**, *399*, 564−566.
(25) Liu, T. *J. Chem. Phys.* **1989**, *90*, 5826−5842.
(26) Hur, J.; Shaqfeh, E.; Larson, R. *J. Rheol.* **2000**, *44*, 713−742.
(27) Doyle, P.; Shaqfeh, E.; Gast, A. *J. Fluid Mech.* **1997**, *334*, 251−291.
(28) Hur, J.; Shaqfeh, E.; Babcock, H.; Smith, D.; Chu, S. *J. Rheol.* **2001**, *45*, 421−450.
(29) Babcock, H.; Smith, D.; Hur, J.; Shaqfeh, E.; Chu, S. *Phys. Rev. Lett.* **2000**, *85*, 2018−2021.
(30) Bustamante, C.; Marko, J.; Siggia, E.; Smith, S. *Science* **1994**, *265*, 1599−1600.
(31) Quake, S.; Babcock, H.; Chu, S. *Nature (London)* **1997**, *388*, 151−154.
(32) Perkins, T.; Quake, S.; Smith, D.; Chu, S. *Science* **1994**, *264*, 822−826.
(33) Babcock, H.; Teixeira, R.; Hur, J.; Shaqfeh, E.; Chu, S. *Macromolecules* **2003**, *36*, 4544−4548.
(34) Smith, D.; Chu, S. *Science* **1998**, *281*, 1335−1340.
(35) Perkins, T.; Smith, D.; Chu, S. *Science* **1997**, *276*, 2016−2021.
(36) Woo, N.; Shaqfeh, E.; Khomami, B. *J. Rheol.* **2004**, *48*, 299−318.
(37) Hecht, E. *Optics*, 3rd ed.; Addison-Wesley: Reading, MA, 1998.
(38) Schroeder, C.; Teixeira, R.; Shaqfeh, E.; Chu, S. *Macromolecules* **2004**, manuscript in preparation.
(39) Liu, S.; Ashok, B.; Muthukumar, M. *Polymer* **2004**, *45*, 1383−1389.
(40) Hur, J.; Shaqfeh, E.; Babcock, H.; Chu, S. *Phys. Rev. E* **2002**, *66*, 011915−011915.
(41) Chopra, M.; Larson, R. *J. Rheol.* **2002**, *46*, 831−862.
(42) Woo, N.; Shaqfeh, E. *J. Chem. Phys.* **2003**, *119*, 2908−2914.
(43) Woo, N.; Shaqfeh, E.; Khomami, B. *J. Rheol.* **2004**, *48*, 281−298.
(44) Lyulin, A.; Adolf, D.; Davies, G. *J. Chem. Phys.* **1999**, *111*, 758−771.
(45) Aust, C.; Hess, S.; Kroger, M. *Macromolecules* **2002**, *35*, 8621−8630.
(46) Xu, G.; Ding, J.; Yang, Y. *J. Chem. Phys.* **1997**, *107*, 4070−4084.
(47) Smith, D.; Perkins, T.; Chu, S. *Macromolecules* **1996**, *29*, 1372−1373.
(48) Jendrejack, R.; de Pablo, J.; Graham, M. *J. Chem. Phys.* **2002**, *116*, 7752−7759.
(49) Magda, J.; Lee, C.; Muller, S.; Larson, R. *Macromolecules* **1993**, *26*, 1696−1706.
(50) Bird, R. B.; Curtiss, C. F.; Armstrong, R. C.; Hassager, O. *Dynamics of Polymeric Liquids*, 2nd ed.; Wiley: New York, 1987; Vol. 1.
(51) Jeffery, G. B. *Proc. R. Soc. London Ser. A* **1922**, *102*, 161.
(52) Bretherton, F. P. *J. Fluid Mech.* **1962**, *14*, 284−304.
(53) Trevelyan, B.; Mason, S. *J. Colloid Sci.* **1951**, *6*, 354−367.
(54) Schroeder, C.; Teixeira, R.; Shaqfeh, E.; Chu, S. Manuscript in preparation.

MA048077L